Discontinuous Galerkin Methods for the Time-Domain Maxwell's Equations

An Introduction

J.S. Hesthaven[†] and T. Warburton[‡]

[†] *Division of Applied Mathematics, Brown University, Box F, Providence, RI 02912, USA*
[‡] *Department of Mathematics and Statistics, University of New Mexico, Albuquerque, NM 87131, USA*

E-mail: Jan.Hesthaven@brown.edu; timwar@unm.edu

We discuss the basic elements of the discontinuous Galerkin methods for the time-domain Maxwell's equations. A one-dimensional example is developed in detail from which the extension to two- and three-dimensional algorithms are minimal. A few examples are offered as well as guidelines for extensions, generalizations, and helpful software resources.

1. INTRODUCTION

The simplicity, robustness, and reasonable accuracy of the classical finite-difference time-domain (FDTD) method [27] for solving the time-domain Maxwell's equations has propelled this method to become the method of choice among engineers and scientist solving Maxwell's equations in the time-domain. In particular the last decade has seen an explosion in applications and developments, many driven by the very influential texts by Taflove [24, 25].

By now it is also, however, clear that the FDTD methods have severe limitations, e.g., its inherent 2nd order accuracy severely limits their ability to correctly represent wave motion over long distances unless the grid is prohibitively fine. Furthermore, the simplicity of the method, on one hand its very strength, also becomes its most severe restriction by prohibiting the accurate representation of problems in complex geometries. In recent years, a number of efforts have been aimed at addressing the shortcomings of the classical FDTD schemes, e.g., embedding schemes to overcome staircasing [5] and high-order finite difference schemes [25, 14], and body conforming nonorthogonal FDTD methods [15, 6] or contour path methods [18]. Other techniques and improvements are discussed in [24, 25]. Most of these methods, however, have not really penetrated into main stream user community, partly due to their complicated nature and partly because these methods themselves often introduce other complications.

For dealing with complex geometries, one can resort to the use of finite-volume [22]/finite element methods [17, 26], these methods are, in their classic form, 2nd

order accurate as the FDTD method. Furthermore, the finite element method becomes implicit.

For the accurate and efficient modeling of large scale EM applications the shortcomings of low order methods render them impractical due to the need for fine grids to avoid prohibitive error accumulation. However, this understanding of the very source of the limitations also suggest that a high-order time-domain solution technique may offer the efficiency and accuracy required for future large scale CEM modeling capabilities. High-order methods are characterized by being able to accurately represent wave propagation over very long distances, using only a few points per wavelength and with an error accumulation rate that is significantly reduced as compared to 2nd order accurate schemes [21]. For three-dimensional large scale computations, this translates into dramatic reductions in the required computational resources, i.e., memory and execution time, and promises to offer the ability to model problems of a realistic complexity and size.

Traditionally, the development of suitable high-order solution techniques has been held back by the difficulties associated with formulating stable and high-order accurate schemes for solving wave-dominated problems in geometrically complex domains. The recent development of stable discontinuous element/Penalty methods [3] and efficient and accurate ways of representing solutions and operators on triangles and tetrahedra [9, 10, 11, 12] has paved the way for overcoming the restrictions associated with classical high-order methods. In contrast to high-order schemes based on classical finite element techniques, the approach taken here leads to fully explicit schemes.

In the following we provide a step-by-step tutorial on the key components needed to formulate and implement these methods. The methods are, by any measure, more complex that simple FDTD methods. They are not, however, as complex as one could fear, given that they offer choice of arbitrary order of accuracy and support for fully unstructured grids. Furthermore, their very formulation ensures high computational efficiency and excellent parallel performance and the generality to address related problems, e.g., frequency-domain curl-curl equations and nonlinear MHD, with only minor extensions. In the last section we shall discuss generalization and offer some pointers to software resources which should enable a short startup phase.

2. A ONE-DIMENSIONAL DETOUR

As a way of understanding the multi-dimensional scheme for solving Maxwell's equations, let us begin by considering the central elements of the scheme for the one-dimensional Maxwell's equations

$$\varepsilon \frac{\partial E^y}{\partial t} = -\frac{\partial H^z}{\partial x} \quad , \quad \mu \frac{\partial H^z}{\partial t} = -\frac{\partial E^y}{\partial x} \qquad x \in [0, L] = \Omega \ . \tag{1}$$

For simplicity we restrict the attention to a cavity type problem, with PEC boundaries, i.e., $E^y(0,t) = E^y(L,t) = 0$. Generalization to other types of boundaries, e.g, absorbing boundary conditions are straightforward.

For simplicity of the notation, we write Eq.(1) as a conservation law

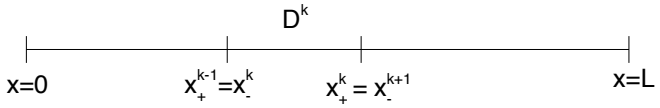

FIG. 1. Notation used in the one dimensional case.

$$\mathrm{Q}\frac{\partial \boldsymbol{q}}{\partial t} + \frac{\partial \boldsymbol{F}(\boldsymbol{q})}{\partial x} = 0 \ ,$$

where

$$\boldsymbol{q} = \begin{bmatrix} E^y \\ H^z \end{bmatrix} \ , \ \boldsymbol{F}(\boldsymbol{q}) = \begin{bmatrix} H^z \\ E^y \end{bmatrix} \ , \ \mathrm{Q} = \begin{bmatrix} \varepsilon & 0 \\ 0 & \mu \end{bmatrix} \ ,$$

represent the statevector of unknown fields, the flux and the materials, respectively.

We shall now assume that the domain of interest, $\Omega = [0, L]$, is segmented into K non-overlapping elements, each covering $x \in [x_-^k, x_+^k]$ and with $x_-^1 = 0$ and $x_+^K = L$, as illustrated in Fig. 1. Furthermore, we shall call the length of each element, $h^k = x_+^k - x_-^k$. With this, we construct a simple linear mapping

$$x^k(r) = x_-^k + \frac{r+1}{2}h^k \ ,$$

such that $r \in [-1, 1]$ represents a standard element of length 2.

In each of the K elements, we shall assume that the solution $\boldsymbol{q}^k(x,t) = [E^y(x^k,t), H^z(x^k,t)]^T$ can be expressed as a polynomial as

$$\boldsymbol{q}^k(x,t) = \sum_{i=0}^{N} \boldsymbol{q}^k(x_i^k,t) l_i^k(r(x)) = \sum_{i=0}^{N} \boldsymbol{q}_i^k(t) l_i^k(x^k) \ ,$$

where x_i^k represent $N+1$ grid points within the k'th element and $l_i^k(x)$ is the classical Lagrange polynomial based on these grid points, i.e.,

$$l_i^k(x) = \prod_{j=0; j\neq i}^{N} \frac{x^k - x_j^k}{x_i^k - x_j^k} \ , \ l_i^k(x_j^k) = \delta_{ij} \ .$$

Rather than using this formula, and to maintain generality, we express the local Lagrange polynomials through the following relation

$$\boldsymbol{q}^k(x,t) = \sum_{i=0}^{N} \boldsymbol{q}_i^k(t) l_i^k(x^k) = \sum_{n=0}^{N} \hat{\boldsymbol{q}}_n^k(t) \phi_n(x^k) \ ,$$

where $\phi_n(x^k)$ is a polynomial basis defined on the interval and $\hat{\boldsymbol{q}}_n^k(t)$ are the expansion or modal coefficients. While many choices are possible, e.g., a simple monomial basis, $\phi_n(x) = x^n$, for computational reasons one should use an orthonormal basis such as

$$\phi_n(x) = \frac{P_n(x)}{\sqrt{2n+1}} \ ,$$

where $P_n(x)$ represent the classical Legendre polynomial [23]. Now defining the matrix

$$\mathrm{V}_{ij} = P_j(x_i) \ ,$$

where x_j are the Legendre Gauss Lobatto quadrature points, we recover

$$\boldsymbol{q}_N^k = \mathrm{V}\hat{\boldsymbol{q}}_N^k \ , \ \mathrm{V}^T\boldsymbol{l}^k(x^k) = \boldsymbol{\phi}(x^k) \ ,$$

where

$$\boldsymbol{q}_N^k = \left[\boldsymbol{q}_0^k, \ldots, \boldsymbol{q}_N^k\right]^T \ , \ \hat{\boldsymbol{q}}_N^k = \left[\hat{\boldsymbol{q}}^k, \ldots, \hat{\boldsymbol{q}}_N^k\right]^T \ ,$$

are simply vectors of nodal and modal values and

$$\boldsymbol{l}^k(x) = [l_0^k(x^k), \ldots, l_N^k(x^k)]^T \ , \ \boldsymbol{\phi}(x^k) = [\phi_0(x^k), \ldots, \phi_N(x^k)]^T \ ,$$

simply represent the vector of local Lagrange polynomials and polynomial basis functions evaluated at x^k.

In this approach, the matrix V, plays a central role as the transformation between nodal values, $\boldsymbol{q}_N^k$, and modal coefficients, $\hat{\boldsymbol{q}}_N^k$, as well as a way by which to evaluate the Lagrange polynomials. In this one-dimensional case, this may seem as an unnecessarily complicated way of doing this. However, as we shall see shortly, the advantage of this approach is that it generalizes to higher dimensions and general distributions of grid points.

To arrive at the semi-discrete scheme, let us now require that local residual, i.e., the error when $\boldsymbol{q}_N^k$ is substituted into Eq.(1), vanishes in the following way

$$i \in [0, \ldots, N] \ : \ \int_{x_-^k}^{x_+^k} \left(\mathrm{Q}\frac{\partial \boldsymbol{q}_N^k}{\partial t} + \frac{\partial \boldsymbol{F}(\boldsymbol{q}_N^k)}{\partial x} \right) l_i^k(x)\, dx = 0 \ .$$

This can be recognized as a Galerkin approach, albeit on the local element only. Integration by parts once yields

$$\int_{x_-^k}^{x_+^k} \left(\mathrm{Q}\frac{\partial \boldsymbol{q}_N^k}{\partial t} l_i^k(x) - \hat{\boldsymbol{n}} \cdot \boldsymbol{F}(\boldsymbol{q}_N^k) \frac{dl_i^k}{dx} \right) dx = - \oint_{x_-^k}^{x_+^k} \hat{\boldsymbol{n}} \cdot \boldsymbol{F}(\boldsymbol{q}_N^k) l_i^k(x)\, dx \ ,$$

which one can recognize as the weak Galerkin form. Here $\hat{\boldsymbol{n}}$ represent an outward pointing normal vector which, in this one-dimensional case, simply takes the values of ∓ 1 at x_-^k and x_+^k, respectively.

To complete the scheme, we must recognize that two neighboring elements will both contain the same point, e.g., $x_+^k = x_-^{k+1}$, see Fig. 1. Thus, at this point we will have two solutions and we must choose which one, or a combination of the two, is the correct. For this we shall use a numerical flux, $\boldsymbol{F}^*$,

$$\hat{\boldsymbol{n}} \cdot \boldsymbol{F}^* = \hat{\boldsymbol{n}} \cdot \boldsymbol{F}^*(\boldsymbol{q}^-, \boldsymbol{q}^+) \ ,$$

where $\boldsymbol{q}^-$ refers to the local solution and $\boldsymbol{q}^+$ the solution in the neighboring elements. There are several possible choices of this function and we return to this issue shortly. It is important to appreciate the importance of this choice as it is the numerical flux which is responsible for combining all local elementwise solution to the global solution.

With the numerical flux introduced on the right hand side to connect the elements, we do integration by parts once more to obtain the final form

$$\int_{x_-^k}^{x_+^k} \left(\mathrm{Q} \frac{\partial \boldsymbol{q}_N^k}{\partial t} + \frac{\partial \boldsymbol{F}(\boldsymbol{q}_N^k)}{\partial x} \right) l_i^k(x)\, dx = \oint_{x_-^k}^{x_+^k} \hat{\boldsymbol{n}} \cdot \left[\boldsymbol{F}(\boldsymbol{q}^-) - \boldsymbol{F}^* \right] l_i^k(x)\, dx \ . \tag{2}$$

To simplify matters further, assume that $\mathrm{Q}(x)$, i.e., the material coefficients, can be taken to be constant on each element and let us define

$$\mathrm{M}_{ij}^{1d} = \int_{x_-^k}^{x_+^k} l_i^k(x^k) l_j^k(x^k) dx^k = \frac{h^k}{2} \int_{-1}^{1} l_i(r) l_j(r) dr \ ,$$

$$\mathrm{S}_{ij} = \int_{x_-^k}^{x_+^k} l_i^k(x^k) \frac{dl_j}{dx} dx^k = \int_{-1}^{1} l_i(r) \frac{dl_j}{dr} dr \ ,$$

as the one-dimensional mass matrix and stiffness matrix. Note in particular that due to the mapping, the matrices are the same for all elements up to a scaling constant, i.e., only one copy should be stored.

Using the transformation matrix, V, introduced above we immediately obtain

$$\mathrm{M}^{1d} = \left(\mathrm{V}^{-1} \right)^T \mathrm{V}^{-1} \ , \ \mathrm{S} = \left(\mathrm{V}^T \right)^{-1} \mathrm{W} \mathrm{V}^{-1} \ , \ \mathrm{W}_{ij} = \int_{-1}^{1} \phi_i(r) \phi_j'(r) dr \ ,$$

where the latter integrals can be computed by quadrature or by using properties of the orthogonal polynomials.

Before writing down the final scheme, let us discuss choices of the numerical flux, $\boldsymbol{F}^*$. As this flux is responsible for combining the local solutions into a global solution, these choices are clearly important.

One natural condition is that the resulting scheme must be consistent, i.e, the exact solution must satisfy the scheme when refining the grid. A simple central flux would ensure this, i.e.,

$$\hat{\boldsymbol{n}} \cdot \boldsymbol{F}^*(\boldsymbol{q}^-, \boldsymbol{q}^+) = \frac{1}{2} \left[\boldsymbol{F}(\boldsymbol{q}^+) + \boldsymbol{F}(\boldsymbol{q}^-) \right] \ .$$

The advantage of this choice is its simplicity and energy conservation. However, for general (multidimensional) problems an upwind flux is superior. To derive this numerical flux one takes advantage of the fact that Maxwell's equations propagates waves around and, at any point, one can always determine which way information is propagating by considering characteristic variables. This yields

$$\hat{\boldsymbol{n}} \cdot \boldsymbol{F}^* = \frac{1}{2} \begin{cases} \overline{Z}^{-1} \left(\hat{n}_x \{ Z H^z \} + [\![E^y]\!] \right) \\ \overline{Y}^{-1} \left(\hat{n}_x \{ Y E^y \} + [\![H^z]\!] \right) \end{cases} , \tag{3}$$

where $[\![q]\!] = q^- - q^+$ represent the local jump in function value and $\{q\} = q^+ + q^-$. The material parameters of the problem are given by

$$Z^{\pm} = \sqrt{\frac{\mu^{\pm}}{\varepsilon^{\pm}}} \ , \ Y^{\pm} = \left(Z^{\pm} \right)^{-1} \ ,$$

represent the local impedance and conductance with the average values

$$\overline{Z} = \frac{Z^+ + Z^-}{2} \ , \ \overline{Y} = \frac{Y^+ + Y^-}{2} \ .$$

Combining Eq.(2) with the upwind flux, Eq.(3), and the definition of the matrix operators above yields the local semi-discrete scheme

$$\begin{aligned} \varepsilon^k \frac{h^k}{2} \mathrm{M}^{1d} \frac{d\boldsymbol{E}_N^k}{dt} + \boldsymbol{S}\boldsymbol{H}_N^k = & \quad \boldsymbol{e}_0 \left[\frac{1}{\overline{Z}} \left(-Z^+ [\![\boldsymbol{H}_N^k]\!] - [\![\boldsymbol{E}_N^k]\!] \right) \right]_{x_-^k} \\ + & \quad \boldsymbol{e}_N \left[\frac{1}{\overline{Z}} \left(Z^+ [\![\boldsymbol{H}_N^k]\!] - [\![\boldsymbol{E}_N^k]\!] \right) \right]_{x_+^k} , \end{aligned} \tag{4}$$

$$\begin{aligned} \mu^k \frac{h^k}{2} \mathrm{M}^{1d} \frac{d\boldsymbol{H}_N^k}{dt} + \boldsymbol{S}\boldsymbol{E}_N^k = & \quad \boldsymbol{e}_0 \left[\frac{1}{\overline{Y}} \left(-Y^+ [\![\boldsymbol{E}_N^k]\!] - [\![\boldsymbol{H}_N^k]\!] \right) \right]_{x_-^k} \\ + & \quad \boldsymbol{e}_N \left[\frac{1}{\overline{Y}} \left(Y^+ [\![\boldsymbol{E}_N^k]\!] - [\![\boldsymbol{H}_N^k]\!] \right) \right]_{x_+^k} . \end{aligned} \tag{5}$$

Here $(\boldsymbol{E}_N^k, \boldsymbol{H}_N^k)$ are the vectors of locally unknown fields on element k and $\boldsymbol{e}_i$ is a N+1 long i'th unit vector. Also $[\ \cdot\ ]_a$ refers to evaluation of what is inside the bracket at $x = a$.

Since M^{1d} is entirely local, it can be inverted initially, making the semi-discrete scheme fully explicit. Furthermore, the discontinuous nature of the formulation is trivially parallel, essential to address large scale problems. We also note that all operations can be cast as simple matrix-vector (or in the case of many elements, matrix-matrix) operations which are both straightforward to implement and offers high performance.

Equations (4)-(5) represents the basic scheme at all interior element interfaces. At the metallic outer boundaries, one simply defines

$$E_+^0 = -E_-^1 \quad , \quad H_+^0 = H_-^1 \quad ,$$

and likewise at the right end, i.e., one is imposing the Dirichlet conditions by a simple mirror principle.

Without going into details, one can prove the following error estimate for the above scheme [11]

$$\|\boldsymbol{q}(t) - \boldsymbol{q}_N(t)\| \leq \frac{h^\sigma}{N^s}\|\boldsymbol{q}(0) - \boldsymbol{q}_N(0)\|_s + t\frac{h^{\sigma-1}}{N^{s-2}} \max_{t\in[0,T]} \|\boldsymbol{q}(t)\|_s \quad . \tag{6}$$

Here $\|\cdot\|$ is the global energy norm, $\|\cdot\|_s$ is the energy norm of the first s-derivatives (the Sobolev norm), and $\sigma = \max(s, N+1)$, while h is maximum element length, h^k.

Thus if the solution, $\boldsymbol{q}$, is smooth, i.e., $\|q\|_s$ is bounded for high values of s, we have hp-convergence. Furthermore, the error can grow at most linearly in time and the growth rate decays rapidly with increasing order.

This highlights the advantages of this method with general order elements, N, of general length h and with a very slow error accumulation of time, making it ideally suited for long time integration problems.

The semi-discrete scheme, Eqs.(4)-(5), can be written schematically as

$$\frac{d\boldsymbol{q}_N}{dt} = \boldsymbol{G}(\boldsymbol{q}_N, t) \quad ,$$

i.e., it is simply a system of ordinary differential equations. These can be solved using a variety of different methods, with a popular choice being a standard 4th order explicit Runge-Kutta scheme

$$\begin{aligned}
\boldsymbol{K}_1 &= \boldsymbol{G}(\boldsymbol{q}_N(t), t) \\
\boldsymbol{K}_2 &= \boldsymbol{G}(\boldsymbol{q}_N(t) + 0.5\Delta t\boldsymbol{K}_1, t + 0.5\Delta t) \\
\boldsymbol{K}_3 &= \boldsymbol{G}(\boldsymbol{q}_N(t) + 0.5\Delta t\boldsymbol{K}_2, t + 0.5\Delta t) \\
\boldsymbol{K}_4 &= \boldsymbol{G}(\boldsymbol{q}_N(t) + \Delta t\boldsymbol{K}_3, t + \Delta t) \\
\boldsymbol{q}_N(t+\Delta t) &= \boldsymbol{q}_N(t) + \frac{\Delta t}{6}\left(\boldsymbol{K}_1 + 2\boldsymbol{K}_2 + 2\boldsymbol{K}_3 + \boldsymbol{K}_4\right) \quad .
\end{aligned}$$

A rigorous expression for the stable time step, Δt, is not known, but good estimate is

$$\Delta t \leq \mathrm{CFL} \min_\Omega \sqrt{\varepsilon^k \mu^k}\Delta x^k = \mathrm{CFL} \min_\Omega \sqrt{\varepsilon^k \mu^k} h^k \Delta r \quad ,$$

with CFL being of $\mathcal{O}(1)$ and $min\Delta r \simeq CN^{-2}$.

To illustrate the performance of the above scheme, let us consider the simple test case of a metallic cavity, $x \in [-1, 1]$, filled with two different nonmagnetic materials. The material interface is assumed to be at $x = 0$ and the two materials have $\varepsilon_r = 1.0$ and $\varepsilon_r = 2.25$ respectively. The exact solution is well known [5].

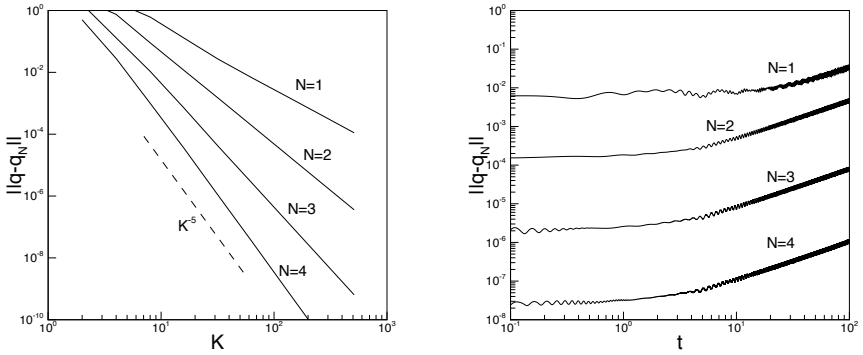

FIG. 2. On the left is shown the global error at final time $T = 1$ for the one-dimensional cavity problem solved using K elements, each with N'th order polynomials. On the right is shown the time-dependence of the error with $K = 64$ elements, confirming linear growth.

In Fig. 2 we illustrate the accuracy of the computed solution at $T = 1$, confirming the essence of the error estimate given in Eq.(6, i.e., both h ($= K^{-1}$, decreasing the grid size) and p (increasing the local polynomial order) convergence is achieved. In Fig. 2 we also illustrate the very limited accumulation of errors over time, in accordance with the above result.

This all suggests that these methods are well suited for situations where

- High-accuracy and large dynamic range in solution is required
- Long time integration is needed
- Electrically large problems, requiring minimal points per wavelength to achieve a reasonable accuracy.

These are clearly all properties of relevance to problems of the future and, more pressing perhaps, for many current technology problems.

Furthermore, as we shall discuss in the following, the approach outlined for the very simple one-dimensional problem generalizes with minimal changes to problems requiring three-dimensional fully unstructured grids and very complex, realistic geometries.

3. EXTENSION TO TWO DIMENSIONS

With the detailed derivation of the one-dimensional scheme above, the extension to two- (or three-) dimensional problems is relatively straight forward. In the following we shall highlight the general approach to see the similarities and minor differences.

For simplicity, we consider the two-dimensional form of Maxwell's equations, e.g.,

$$\begin{aligned} \varepsilon \frac{\partial E^x}{\partial t} &= \frac{\partial H^z}{\partial y} \ , \\ \varepsilon \frac{\partial E^y}{\partial t} &= -\frac{\partial H^z}{\partial x} \ , \\ \mu \frac{\partial H^z}{\partial t} &= \frac{\partial E^x}{\partial y} - \frac{\partial E^y}{\partial x} \ , \end{aligned} \tag{7}$$

known as the TE form. The dual form is found simply by substituting (E^x, E^y, H^z) with $(H^x, H^y, -E^z)$ and exchange ε and μ. This yields the TM form.

In both cases we have

$$\hat{\boldsymbol{n}} \times [\![\boldsymbol{E}]\!] = \hat{\boldsymbol{n}} \times [\![\boldsymbol{H}]\!] = 0 \ ,$$

i.e., tangential continuity, at all nonmetallic interfaces. At a PEC boundary

$$\hat{\boldsymbol{n}} \times \boldsymbol{E} = \hat{\boldsymbol{n}} \cdot \boldsymbol{H} = 0 \ .$$

In both cases, $\hat{\boldsymbol{n}}$ represents an outward pointing normal vector.

3.1. The Nodal Element

The key difference between the one-dimensional and the multidimensional scheme is that the latter has to allow for the modeling of problems in geometrically complex settings, i.e., it does not suffice to consider simple dimension-by-dimension extensions of the one-dimensional approach.

To ensure this geometric flexibility, we assume that the computation domain, Ω, can be filled by some standard element, D^k, e.g., triangles or quadrilaterals. We shall furthermore assume that this multi-element grid is performed in a geometry and material conforming way, i.e., elements are assumed to have edges aligned with material/metallic interfaces.

Following the one-dimensional approach, it is clear that with the local element, D^k, we should seek an orthogonal polynomial basis, $\phi_i(\boldsymbol{x})$, as well as a set of grid points, $\boldsymbol{x}_i^k \in \mathsf{D}^k$. For the quadrilateral, one could simply use a dimension-by-dimension extension of the one-dimensional case. Let us therefore focus on the case of triangles which also has the main interest due to its geometric flexibility, possibility of utilizing existing finite element/finite volume grid generation software, and ease of exploring adaptive strategies.

The number of grid points needed per triangle is

$$N = \frac{(n+1)(n+2)}{2} \ ,$$

which also becomes the number of local unknowns. Here n is the order of the local polynomial approximation. The question we must address is where to put these grid points, e.g., there is no obvious extension of the one-dimensional case.

As for the one dimensional case we shall assume the existence of a mapping which maps the standard right angle triangle, $\mathsf{I} : \{(r,s) \in [-1,1]; r+s \leq 0\}$, to

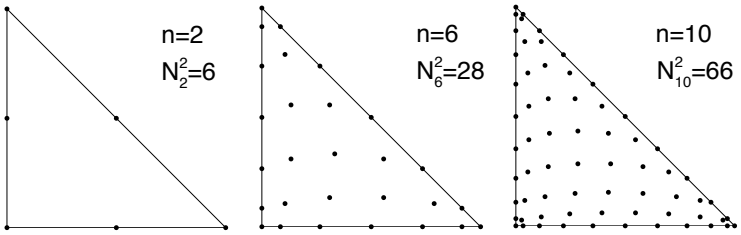

FIG. 3. Examples of nodal distributions in the triangle for different orders, n, of approximation. N_n^2 lists the total number of grid points.

the particular triangle, D^k. Assuming for simplicity that D^k is straightsided, this mapping is simply given as

$$\boldsymbol{x}^k(r,s) = -\frac{r+s}{2}\boldsymbol{v}_1^k + \frac{1+r}{2}\boldsymbol{v}_2^k + \frac{1+s}{2}\boldsymbol{v}_3^k \ , \tag{8}$$

where $\boldsymbol{v}_i^k$ represent the 3 vertices of D^k and $(r,s) \in \mathsf{I}$ are the coordinates in the standard triangle while $\boldsymbol{x}^k \in \mathsf{D}^k$. From this simple map, we can compute the metric of the mapping, needed for computing derivatives as we shall see shortly, as well as the transformation Jacobian. An important observation to make is that the transformation Jacobian, J, is a constant for any straightsided triangle, D^k. The details are all given in [9, 10] and is essentially a generalization of the one-dimensional case.

The choice of the nodal distributions inside the triangle has received some attention recently and such distributions, allowing for the construction of well behaved unique Lagrange polynomials up to order 19, can be found in [8]. There are exactly N grid points in a triangle and, furthermore, the nodes along the edges are the one dimensional Legendre Gauss Lobatto points, also used in Sec. 2. A few examples of how the grid point distributions look like are shown in Fig. 3.

An orthonormal basis on the triangle is given as [20]

$$\tilde{\psi}_i(\boldsymbol{r}) = P_{\alpha_1}^{(0,0)}\left(\frac{2(r+1)}{(1-s)} - 1\right)\left(\frac{1-s}{2}\right)^{\alpha_1} P_{\alpha_2}^{(2\alpha_1+1,0)}(s) \ ,$$

$$i = \alpha_1 + n\alpha_2 - \frac{\alpha_2}{2}(-1+\alpha_2) + 1 \ ,$$

$$\gamma_i = \left(\frac{2}{2\alpha_1+1}\right)\left(\frac{1}{\alpha_1+\alpha_2+1}\right) \ ,$$

$$\psi_i(\boldsymbol{r}) = \frac{\tilde{\psi}_i(\boldsymbol{r})}{\sqrt{\gamma_i}} \ . \tag{9}$$

$P_n^{(\alpha,\beta)}(x)$ represents the classical Jacobi polynomial of order n [23], e.g., $P_n^{(0,0)}(x)$ is the Legendre polynomial also used in the one dimensional case.

This may seem a bit complicated. However, there are standard ways of computing/evaluating Jacobi polynomials and software for doing so can be found from online sources (see Sec. 5).

With this, all essential operators, i.e., mass and stiffness matrices as well as the transformation matrix V, can be defined and generated exactly as in the one-dimensional case discussed in the above.

3.2. The Scheme

With the local elementwise treatment in place, we can continue the development of the global scheme. As in the one dimensional case, we write, for simplicity, Maxwell's equations as

$$\mathrm{Q}\frac{\partial \boldsymbol{q}}{\partial t} + \nabla \cdot \boldsymbol{F}(\boldsymbol{q}) = 0 \ ,$$

where Q represent the materials, $\boldsymbol{q}$ the 3-vector of fields and $\boldsymbol{F}(\boldsymbol{q})$ the flux. The detailed definition of these depends on which polarization is considered, i.e., for the TE form we have

$$\mathrm{Q} = \begin{bmatrix} \varepsilon & 0 & 0 \\ 0 & \varepsilon & 0 \\ 0 & 0 & \mu \end{bmatrix} \ , \quad \boldsymbol{q} = \begin{bmatrix} E^x \\ E^y \\ H^z \end{bmatrix} \ , \quad \boldsymbol{F}(\boldsymbol{q}) = \begin{bmatrix} 0 & -H^z \\ H^z & 0 \\ E^y & -E^x \end{bmatrix} \ .$$

Exactly as in the one dimensional case we shall require that the polynomial approximation

$$\boldsymbol{q}_N^k(\boldsymbol{x}, t) = \sum_{i=1}^{N} \boldsymbol{q}^k(\boldsymbol{x}_i^k, t) L_i^k(\boldsymbol{x}^k) \ ,$$

satisfies the equation as

$$\forall k \ : \quad \int_{\mathsf{D}^k} \left(\mathrm{Q}\frac{\partial \boldsymbol{q}_N^k}{\partial t} + \nabla \cdot \boldsymbol{F}_N^k \right) L_i^k(\boldsymbol{x}^k) \, d\boldsymbol{x}^k = \oint_{\partial \mathsf{D}^k} L_i^k(\boldsymbol{x}^k) \hat{\boldsymbol{n}} \cdot \left[\boldsymbol{F}_N^k - \boldsymbol{F}^* \right] \, d\boldsymbol{x}^k \ . \tag{10}$$

Specifying the numerical flux, $\hat{\boldsymbol{n}} \cdot \boldsymbol{F}^*$, follows exactly the same lines as in the one-dimensional case, i.e., a central flux is obtained directly from the average of the two fluxes while the upwind flux can be derived from the general three-dimensional expression

$$\hat{\boldsymbol{n}} \cdot [\boldsymbol{F} - \boldsymbol{F}^*] = \begin{cases} \overline{Z}^{-1} \boldsymbol{n} \times (-Z^+ [\![\boldsymbol{H}]\!] + \boldsymbol{n} \times [\![\boldsymbol{E}]\!]) \\ \overline{Y}^{-1} \boldsymbol{n} \times (Y^+ [\![\boldsymbol{E}]\!] + \boldsymbol{n} \times [\![\boldsymbol{H}]\!]) \end{cases} \ . \tag{11}$$

This suffices to write down the local two-dimensional scheme for TE scheme as

$$\varepsilon^k J^k \mathrm{M}^{2d} \frac{\partial \boldsymbol{E}_N^x}{\partial t} - \mathrm{S}_y \boldsymbol{H}_N^z = \mathrm{F} \left[\frac{\hat{n}_y}{\overline{Z}} \left(-Z^+ [\![\boldsymbol{H}_N^z]\!] + [\![\boldsymbol{E}_T]\!] \right) \right] \ , \tag{12}$$

$$\varepsilon^k J^k \mathrm{M}^{2d} \frac{\partial \boldsymbol{E}_N^y}{\partial t} + \mathrm{S}_x \boldsymbol{H}_N^z = \mathrm{F} \left[\frac{\hat{n}_x}{\overline{Z}} \left(Z^+ [\![\boldsymbol{H}_N^z]\!] - [\![\boldsymbol{E}_T]\!] \right) \right] \ ,$$

$$\mu^k J^k \mathrm{M}^{2d} \frac{\partial \boldsymbol{H}_N^z}{\partial t} - \mathrm{S}_y \boldsymbol{E}_N^x + \mathrm{S}_x \boldsymbol{E}_N^y = \mathrm{F} \left[\frac{1}{\overline{Y}} \left(Y^+ [\![\boldsymbol{E}_T]\!] + [\![\boldsymbol{H}_N^z]\!] \right) \right] \quad .$$

Here $(\boldsymbol{E}_N^x, \boldsymbol{E}_N^y, \boldsymbol{H}_N^z)$ represent the N-long vectors of unknowns on the element D^k and we have defined $\boldsymbol{E}_T = \hat{\boldsymbol{n}} \times \boldsymbol{E}$ as the tangential component of $\boldsymbol{E}$ along the boundary of the element. Furthermore, (ε^k, μ^k) represent the local material parameters and J^k represents the local transformation Jacobian, recovered from Eq.(8).

Most of what remains in the above translates exactly from the one-dimensional case, e.g., M^{2d} represents the local mass matrix constructed directly from V; the stiffness matrices S_x and S_y are given as

$$\mathrm{M}^{2d} = \left(\mathrm{V}^{-1} \right)^T \mathrm{V}^{-1} \quad .$$

$$\mathrm{S}_r = \left(\mathrm{V}^T \right)^{-1} \mathrm{W}^r \mathrm{V}^{-1} \quad , \quad \mathrm{W}_{ij}^r = \int_{\mathsf{D}^k} \phi_i(\boldsymbol{r}) \frac{\partial \phi_j(\boldsymbol{r})}{\partial dr} d\boldsymbol{r} \quad ,$$

$$\mathrm{S}_s = \left(\mathrm{V}^T \right)^{-1} \mathrm{W}^s \mathrm{V}^{-1} \quad , \quad \mathrm{W}_{ij}^s = \int_{\mathsf{D}^k} \phi_i(\boldsymbol{r}) \frac{\partial \phi_j(\boldsymbol{r})}{\partial ds} d\boldsymbol{r} \quad ,$$

where $\boldsymbol{r} = (r, s)$ are the local coordinates in the reference element. Using the chain rule this simply yields

$$\mathrm{S}_x = S_r \frac{\partial r}{\partial x} + S_s \frac{\partial s}{\partial x} \quad , \quad \mathrm{S}_y = S_r \frac{\partial r}{\partial y} + S_s \frac{\partial s}{\partial y} \quad ,$$

where the matrix coefficients are obtained directly from the mapping given in Eq.(8).

The main difference between Eqs.(4)-(5) and Eq.(12) is found in the matrix F which is the finite dimensional approximation of the surface integral.

$$\oint_{\partial \mathsf{D}^k} L_i^k(\boldsymbol{x}^k) \hat{\boldsymbol{n}} \cdot \left[\boldsymbol{F}_N^k - \boldsymbol{F}^* \right] d\boldsymbol{x}^k = \oint_{\partial \mathsf{D}^k} L_i^k(\boldsymbol{x}^k) g(\boldsymbol{x}) \, d\boldsymbol{x} \quad ,$$

where $g(\boldsymbol{x})$ has been introduced for simplicity. This clearly breaks into 3 edge integrals ($l = 1, 2, 3$) of the form

$$\oint_{\partial \mathsf{D}_l^k} L_i^k(\boldsymbol{x}^k) g(\boldsymbol{x}) \, d\boldsymbol{x} = \oint_{\partial \mathsf{D}_l^k} l_i^k(\boldsymbol{x}^k) \sum_{j=0}^{n} g(\boldsymbol{x}_j) l_j^k(\boldsymbol{x}^k) \, d\boldsymbol{x} \quad ,$$

where $l_i^k(x)$ is the one-dimensional Lagrange polynomial based on the grid points along the edge l, i.e.,

$$\mathrm{M}_{ij}^{1d} = \oint_{\partial \mathsf{D}_l^k} l_i^k(\boldsymbol{r}^k) l_j^k(\boldsymbol{r}^k) \, d\boldsymbol{r} \quad ,$$

is simply the one-dimensional mass matrix. Note that the two-dimensional Lagrange polynomial, $L_i^k(\boldsymbol{x}^k)$, restricted to the one-dimensional edge reduces the familiar one-dimensional Lagrange polynomial, $l_i^k(\boldsymbol{x}^k)$, due to uniqueness of the polynomials. If we now define the R_l is an $(n+1) \times N$ restriction operator that

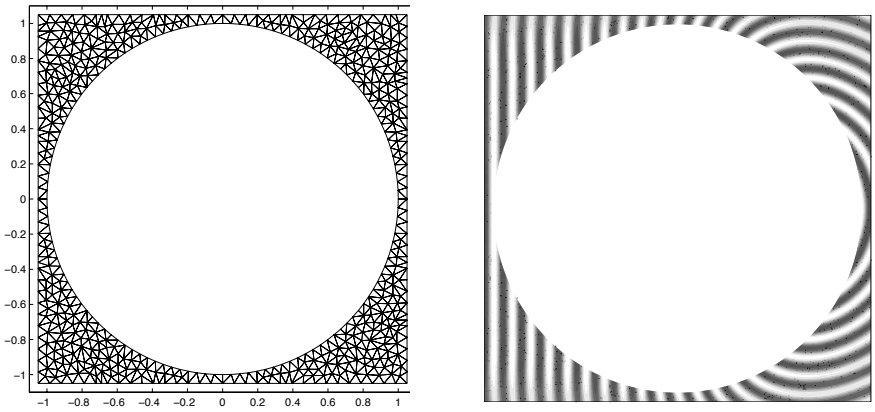

FIG. 4. On the left is shown finite element grid (950 elements) used to model plane wave TM scattering of a $ka = 20\pi$ metallic cylinder. A snapshot of E^z is shown on the right. The computational domain is terminated with high-order global boundary conditions.

extracts the $(n+1)$ nodes along edge l, then the edge integral along edge l is given as

$$\oint_{\partial \mathrm{D}_l^k} L_i^k(\boldsymbol{x}^k) g(\boldsymbol{x})\, d\boldsymbol{x} = s_l \mathrm{R}_l^T \mathrm{M}^{1d} \mathrm{R}_l \boldsymbol{g} \quad ,$$

where s_l is the Jacobian associated with mapping the edge length to the standard interval $[-1, 1]$. The complete operator edge operator then becomes

$$\mathrm{F} = \sum_l s_l \mathrm{R}_l^T \mathrm{M}^{1d} \mathrm{R}_l \quad .$$

Clearly the components of this can be computed a priori for the standard element added with the geometry weights.

The semi-discrete form of the equations, Eq. 12, can be advanced in time using the 4th order Runge-Kutta discussed in the above with a time-step scaling like

$$\Delta t \leq \mathrm{CFL} \min_{\Omega} \sqrt{\varepsilon^k \mu^k} \frac{h}{n^2} \quad ,$$

where h is the smallest edge length of the element.

3.3. A Few Examples

In the following we shall offer a few examples of two- and three-dimensional tests. The emphasis here is on evaluation and verification of the scheme. Many other examples, including hard benchmarks and very large scale application, can be found in [11, 12, 14].

As a first, and familiar example, we consider plane wave TM scattering of a $ka = 20\pi$ metallic cylinder. As simple as the case is, it allows for a thorough

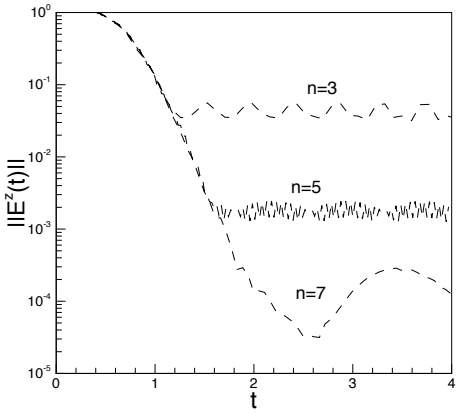

FIG. 5. The error in E^z for plane wave TM scattering by a $ka = 20\pi$ metallic cylinder as a function of time for increasing resolution.

validation through the exact solution. We use 950 elements and an high-order local boundary condition [7]. The grid as well as a snapshot of E^z is shown in Fig. 4.

To measure the accuracy of the solution we compute the error in E^z as a function of time for increasing resolution. The results are shown in Fig. 5. For 5th order polynomials $n = 5$ there are 8-10 points per wavelength. The results confirm exponential convergence as expected. This is also a indication of the excellent performance of the high order local boundary conditions which is introduces errors well below the approximation error.

As a slight more challenging, although still two-dimensional, test case we consider plane wave TM scattering by a 'Pacman' shaped metallic cylinder. The grid, containing approximately 3800 elements, and a snapshot the E^z component is shown in Fig. 6. To truncate computational domain we use in this case a perfectly matched layer [25], to illustrate that one can terminate the domain in a variety of ways as appropriate.

This scattering problem does not have a known exact solution. To estimate the accuracy of the computed result we consider the convergence of the bistatic radar cross section (RCS). In Fig. 7 we show the computed RCS obtained using 3 different orders of approximation, clearly suggesting convergence. This example not only illustrates the ability to solve general problems but also highlights the added flexibility one has by using a high order methods on a general grid. Without having to redo the computational grid, a time consuming process for general geometries, one can obtain a sequence of solutions of increasing accuracy by simply raising the local order of approximation. This dual path to a converged result is one of the significant advantages of a flexible *hp*-type scheme as it decreases the significant complications associated with grid generation. Furthermore, high order elements are found to be significantly more robust to elements with bad aspect ratio.

As a final example, we consider the computation of eigenfrequencies of a $[-1, 1]^3$ PEC air filled cube. The computation is done by initially having a broadband pulse which excite a number resonant frequencies. By doing a Fourier transform of a time

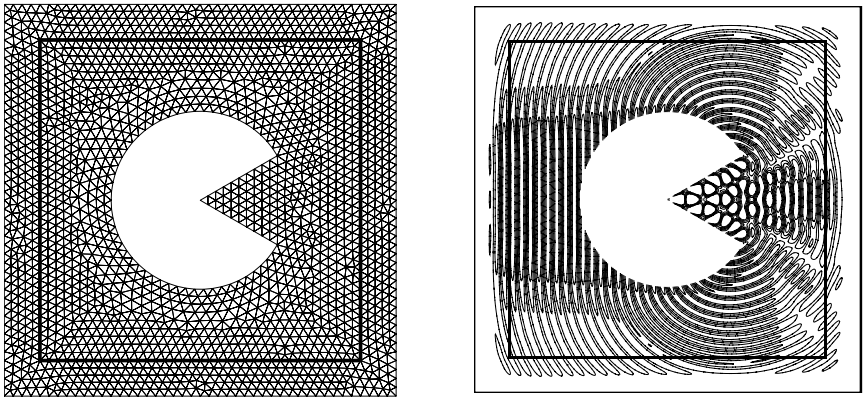

FIG. 6. On the left is shown finite element grid (3800 elements) used to model plane wave TM scattering of a Pacman shaped metallic cylinder. A snapshot of E^z is shown on the right. A Perfectly Matched Layer (PML) is used to terminate the computational domain.

trace one can then compute the resolved modes. In this simple case, the resonant frequencies are given as

$$\omega = \pi\sqrt{m^2+n^2+l^2}; m+n+l \geq 2 \quad .$$

We solve the problem by tiling the cube with 286 tetrahedra, each of 4th order, and advance the initial conditions for 250 fundamental periods. The results are shown in Fig. 8.

The results in Fig. 8 not only confirms that the correct eigenfrequencies are reproduced but also suggests that at least frequencies of $\omega \simeq 20$ is well resolved. This correspond to wave numbers between 6 and 7. With about $K^{1/3} \simeq 6.5$ element per edge and 5 grids points per edge, this corresponds to 4-5 points per wavelength, clearly demonstrating the excellent performance of a high order method even while using a coarse grid.

4. FURTHER EXTENSIONS AND GENERALIZATIONS

The most natural extension of the schemes discussion above is to include full three-dimensional Maxwell's equations. As we have seen in the last example of the previous section this is certainly possible. In fact, going from two- to three-dimensions introduces nothing new from the two-dimensional case discussed in detail in the last section. Once the nodes [9] and the orthogonal polynomials are identified, all the operators can defined and the scheme formulated. The three-dimensional flux is already given in Eq. (11). The only new component is that the F matrix now must correspond to a surface and not a line integral. The details of how to do this as well as numerous examples, further details of implementation, full analysis, and examples of parallel performance are discussed in [11, 12].

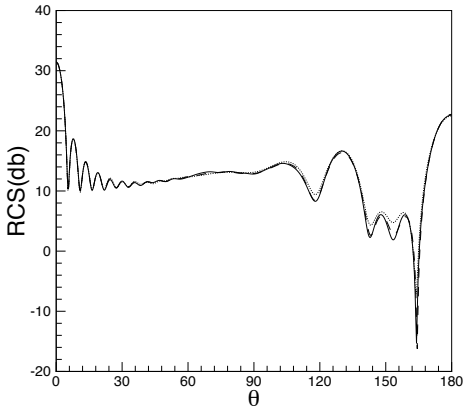

FIG. 7. Bistatic RCS(db) computed for Pacman shaped metallic cylinder in Fig. 6. Computation done using 3rd, 5th, and 7th order approximations and results plotted on same scale, confirming convergence.

The discontinuous Galerkin formulation does not, in contrast to FDTD methods, preserve the divergence free nature of the fields, although the associated error is well controlled and generally negligible. Some efforts have focused on this issue, either by having additional slaved variables which are approximations to divergence free fields [12], or by using a locally divergence free basis [4]. In both cases only local divergence is preserved.

Another relevant issues is that of time stepping, something we dealt with in the above by using a simple 4th order Runge-Kutta method. However, the local nature of the formulation enables the elegant use of local time stepping as discussed in [2]. Other important extensions to deal with locally refined grids are explicit-implicit methods [1] as well as low storage methods [19].

With the significant success of the above methods for solving the time-domain Maxwell's equations, one can speculate whether the same formulation can be used to solve the curl-curl equation of harmonic problems or even eigenvalue problems. Questions of this character has been considered in [13, 16], concluding that this is indeed possible and paves the way for a completely general discontinuous Galerkin approach for solving Maxwell's equations both in frequency and time-domain.

5. CONCLUSIONS AND FURTHER INFORMATION

It has been the intention of this little manuscript to offer an introduction to the formulation and development of discontinuous Galerkin methods for solving the time-domain Maxwell's equations. As we have seen, these methods have matured to a level where their implementation is relatively straightforward and resulting in algorithms which are flexible, efficient, accurate, and robust.

Many further examples and validations can be found in the listed references. Furthermore, at HTTP://WWW.USEME.ORG numerous other examples and animations are displayed. This page also contains examples and extensions of the same essential formulation to enable solution of magnetohydrodynamics and gasdynamics.

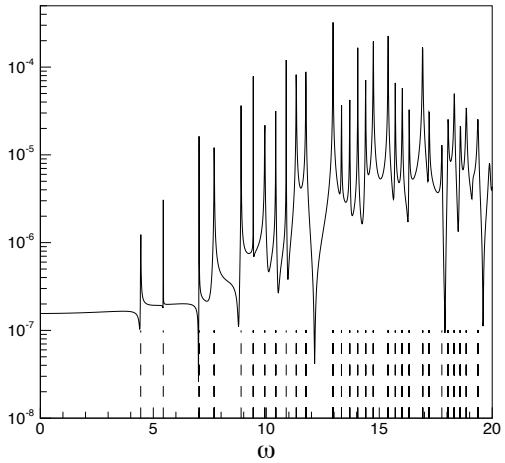

FIG. 8. Eigenfrequencies in a $[-1,1]^3$ PEC cavity, computed by the Fourier transform of a time series of 500 periods. 286 4th order fully unstructured tetrahedral grid was used. The solid line represents the computed spectrum while the vertical dashed lines signify the exact solution, $\omega = \pi\sqrt{m^2+n^2+l^2}; m+n+l \geq 2$.

A small startup company, HyPerComp Inc. (HTTP://WWW.HYPERCOMP.NET) is pursuing the development of a commercial environment based on these techniques.

However, as we all know and appreciate, doing is superior to anything else when it comes to understanding a new idea. For this purpose we implemented both one and two-dimensional versions of the algorithms in Matlab and will make these scripts available to interested parties. The key elements in these implementations are a set of files, one for each order, which contains the nodal coordinates in the standard element, the critical V matrix, the one- and two-dimensional mass matrices, M^{1d} and M^{2d}, the restriction matrix, R, as well as the stiffness matrix, S. This suffices to completely specify the local scheme and should enable a very short startup time in the development and exploration of these methods as it more or less reduces the solution problem to one of grid generation and logistics.

The scripts and files as well as further information can be downloaded from HTTP://WWW.DAM.BROWN.EDU/USEME or by contacting the authors.

ACKNOWLEDGMENT

The work of JSH was partly supported by NSF under contract DMS-0074257, through an NSF Career Award, by ARO under contract DAAD19-01-1-0631, by AFOSR under contract FA9550-04-1-0072, and by the Alfred P. Sloan Foundation through a Sloan Research Fellowship. TW was partially supported by NFS under contract ITR-0324911, through the Sandia-University Research Program, and by ARO under contract DAAD19-03-1-0146.

REFERENCES

1. M. H. Carpenter and C. A. Kennedy, *Fourth order 2N-storage Runge-Kutta scheme*, NASA-TM-109112, NASA Langley Research Center, VA. 1994.
2. C. Chauviere, J. S. Hesthaven, A. Kanevsky, and T. Warburton, *High-Order Localized Time Integration for Grid-Induced Stiffness*. 2nd MIT Conference on Fluid Dynamics, Boston, 2003. Vol II, 1883-1886.
3. B. Cockburn and C.W. Shu, *Runge-Kutta Discontinuous Galerkin Methods for Convection-Dominated Problems*, J. Sci. Comput. **16**(2001), pp. 173-261.
4. B. Cockburn, F. Li, and C.W. Shu, *Locally Divergence Free Discontinuous Galerkin Methods for the Maxwell Equations*, J. Comput. Phys. **194**(2004), pp. 588-610.
5. A. Ditkowski, K. Dridi, and J. S. Hesthaven, *Convergent Cartesian Grid Methods for Maxwell's Equations in Complex Geometries*, J. Comput. Phys. **170**(2001), pp. 39-80.
6. M. Fusco, *FDTD Algorithm in Curvilinear Coordinates*, IEEE Trans. Antennas Propaga. **38**(1990), pp. 76-89.
7. T. Hagstrom and T. Warburton, *A New Auxiliary Variable Formulation of High- Order Local Radiation Boundary Conditions: Corner Compatibility Conditions and Extensions to First Order Systems*, Wave Motion, 2004 – to appear.
8. J. S. Hesthaven, *From Electrostatics to Almost Optimal Nodal Sets for Polynomial Interpolation in a Simplex*, SIAM J. Numer. Anal. **35**(1998), pp. 655-676.
9. J. S. Hesthaven and D. Gottlieb, *Stable Spectral Methods for Conservation Laws on Triangles with Unstructured Grids*, Comput. Methods Appl. Mech. Engin. **175**(1999), pp. 361-381.
10. J. S. Hesthaven and C. H. Teng, *Stable Spectral Methods on Tetrahedral Elements*, SIAM J. Sci. Comput. **21**(2000), pp. 2352-2380.
11. J. S. Hesthaven and T. Warburton, *High-Order Nodal Methods on Unstructured Grids. I. Time-Domain Solution of Maxwell's Equations*, J. Comput. Phys. **181**(2002), pp. 1-34.
12. J. S. Hesthaven and T. Warburton, *High-Order Accurate Methods for Time-domain Electromagnetics*, Comput. Model. Engin. Sci. 2003 – to appear.
13. J. S. Hesthaven and T. Warburton, *High Order Nodal Discontinuous Galerkin Methods for the Maxwell Eigenvalue Problem*, Phil. Trans Royal Soc. London A, 2004 – to appear.
14. J. S. Hesthaven, *High-Order Accurate Methods in Time-Domain Computational Electromagnetics: A Review*, Adv. Imaging Elec. Phys. **127**, pp. 59-123.
15. R. Holland, *Finite Difference Solutions of Maxwells Equations in Generalized Nonorthogonal Coordinates*, IEEE Trans. Nuclear Sci. **30**(1983), pp. 4589-4591.
16. P. Houston, I. Perugia, A. Schneebeli, and D. Schötzau, *Interior Penalty Method for the Indefinite Time-Harmonic Maxwell Equations*, SIAM J. Numer. Anal. 2004 – to appear.
17. J. M. Jin, *The Finite Element Method in Electromagnetics*. John Wiley & Sons, Inc. 1993.
18. T.G. Jurgens, A. Taflove, K. Umashaankar, and T.G. Moore, *Finite-Difference Time-Domain Modeling of Curved Surfaces*, IEEE Trans. Antennas Propaga. **40**(1992), pp. 357-366.
19. C. A. Kennedy and M. H. Carpenter, *Additive Runge-Kutta Schemes for Convection-Diffusion-Reaction Equations*, Appl. Numer. Math. **44**(2003), pp. 139-181.
20. T. Koornwinder, *Two-variable Analogues of the Classical Orthogonal Polynomials* in "Theory and Application of Special Functions", R.A. Askey ed., Academic Press, 1975. pp. 435-495.
21. H. O. Kreiss and J. Oliger, *Comparison of Accurate Methods for the Integration of Hyperbolic Problems*, Tellus **24**(1972), pp. 199-215.
22. A. H. Mohammadian, V. Shankar, and W. F. Hall, *Computation of Electromagnetic Scattering and Radiation using a Time-Domain Finite-Volume Discretization Procedure*, Comput. Phys. Comm. **68**(1991), pp. 175-196.
23. G. Szegö, *Orthogonal Polynomials*. Colloquium Publications **23**, American Mathematical Society, Providence, RI. 1939.
24. A. Taflove, *Computational Electrodynamics. The Finite-Difference Time-Domain Method*. Artech House, Boston, 1995.
25. A. Taflove (Ed.), *Advances in Computational Electrodynamics: The Finite-Difference Time-Domain Method*, Aztech House, Boston, 1998.
26. J.L. Volakis, A. Chatterjee and L. Kempel, *Finite Element Methods for Electromagnetics: Antennas, Microwave Circuits and Scattering Applications*. IEEE Press, 1998.
27. K. S. Yee, *Numerical Solution of Initial Boundary Value Problems involving Maxwells Equations in Isotropic Media*, IEEE Trans. Antennas Propaga. **14**(1966), pp. 302-307.